OpenFOAM® Journal

Volume 5 [Full Papers], Pages 1–16
ISSN: 2753-8168

Modelling thermo-electrohydrodynamic convection in rotating spherical shells using OpenFOAM®

Yann Gaillard[1,*], Peter S. B. Szabo[1], Vadim Travnikov[1], and Christoph Egbers[1]

[1]Department of Aerodynamics and Fluid Mechanics, Brandenburg University of Technology Cottbus-Senftenberg, Siemens-Halske-Ring 15a, 03046 Cottbus, Germany
Email address: yann@gaillard.onl

DOI: https://doi.org/10.51560/ofj.v5.136
Results with version(s): OpenFOAM® v2021, compatible with OpenFOAM® v2312
Repository: https://github.com/AtmoFlow/TEHDBoussinesqPimpleFoam

Abstract. Convection in rotating spherical shells can be considered a simplified analogue of many geophysical and astrophysical flows. Here, we investigate a direct numerical simulation of a dielectric fluid in an electric central force field inducing thermo-electrohydrodynamic (TEHD) convection with numerical methods to obtain an accurate solution of the transport equations describing rotating TEHD convection in a non-isothermally heated spherical shell. The choice of the numerical model is based on the International Space Station Experiment GeoFlow and its successor, AtmoFlow. The numerical methods consist of a custom-developed finite volume solver based on the OpenFOAM® ecosystem that is not limited to any geometric restrictions, a commercially developed finite element method, and a pseudo-spectral method. This study aims to validate a custom-coded finite volume solver for investigating TEHD convection for a parametric study of the AtmoFlow spherical shell experiment. The developed TEHD finite volume solver showed solution errors of 1% or less compared to the other two implemented numerical methods.

1. Introduction

Thermo-electrohydrodynamic (TEHD) convection is induced in a non-isothermal dielectric fluid in a sufficiently strong electric field. Depending on the geometrical properties, such as plate, cylinder, or spherical shell, different thresholds exist to induce a convective flow and are given by the critical Rayleigh number, Ra_C. The critical values of the thresholds and the definition of Ra_C are found in a review by Mutabazi et al. [1]. The first investigation of TEHD convection tracks back to the original experiments of Seftleben and Braun [2–4] in the early to mid-1930s. These experiments considered a gas-filled cylinder where an external field modified and enhanced the heat transport. Since then, the force densities that described the convective transport mechanism were derived, and numerical models were used to define the onset of convection, the convective behaviour, and its similarities to natural convection.

The numerical investigation that followed after the experiments of Senftleben and Braun considered a definition of suitable critical Rayleigh numbers that are comparable to natural convection by linear stability analysis in different geometries, see [5–9] and more complex flow states of larger forcing parameter via the Pseudo Spectral Method (PSM) [8–13], the Finite Volume Method (FVM) [14–19], or the Finite Element Method (FEM) [20] to name a few.

The present work extends the studies of Szabo et al. [18] and Gaillard et al. [21] from a two-dimensional shell to a full spherical system using the FVM technique. In addition, dielectric heating is added to the model compared to the prior studies. The full spherical consideration enables the consideration of inertia wave development, especially in the third dimension, resulting out of system rotation. The latitudinal variation of effective rotation strength and topography-induced vortex stretching or squeezing, e.g. in a rotating spherical shell, can now be fully considered.

The PSM technique is a well-established numerical method used, e.g. in magnetohydrodynamic (MHD) flows in cylindrical and spherical geometries, see [22–25], and known for its robust framework which is less

* Corresponding author

Received: 12 March 2024, Accepted: 5 December 2024, Published: 10 January 2025

computational intense. A great advantage is that it provides an easy implementation of rotational forcing in spherical shell geometries that are considered as a simplified analogue of astrophysical and geophysical flows with central force fields, like terrestrial gravity, are of importance [24]. Hence, this particular method served not only in MHD but also in TEHD, see [12, 13]. So far, the PSM method has provided complementary numerical results for the International Space Station experiment GeoFlow, a spherical shell system used to study planetary interiors by an electric force field [8, 9, 26–29]. However, the use of the PSM technique is mostly implemented and performs significantly better for axisymmetric domains, and less complex boundary conditions. Using the FVM method, one of the most common numerical methods in computational fluid dynamics, provides vast pre-processing and post-processing methods, especially in the OpenFOAM® ecosystem. Numerical tools such as OpenFOAM® [30] enable complex mesh geometries and easy implementation of additional multiphysical requirements. This is the case for complex flows, where additional source terms and equations to the overall transport equations must be solved, or the system is composed of multiregions. The FVM is in contrast to PSM, a valid alternative technique, see Zaussinger et al. [31], which performed numerical simulations for the successor of the GeoFlow experiment, the AtmoFlow spherical shell experiment used to study the analogy of planetary atmospheres in a spherical shell system. However, all these solvers need adequate numerical benchmark solutions, especially for custom-coded solvers, which is provided in this study to ensure the multiphysics problem is solved correctly.

1.1. **Aims and objectives.** The aim of this study is to provide a benchmark solution for rotating spherical shell convection with an applied electric central force field to induce TEHD convection, providing an analogy to terrestrial gravity of planets [17]. For this particular task, we propose an FVM solver based on the PIMPLE algorithm, which is a combination of the Semi-Implicit Method for Pressure Linked Equations (SIMPLE) algorithm and the Pressure Implicit with Split Operator (PISO) algorithm within the OpenFOAM® ecosystem. A more detailed explanation of the solver is given in the numerical methods section 3.1. The FVM solver is not restricted to spherical shell systems and is able to model other geometrical entities without further modification. The composition of the solver is designed to enable further development in the OpenFOAM® environment, including multi-region and multiphysics for more complex cases [32]. A sample case and a manual of the solver are found via the URL linked to the GitHub repository.

The benchmark exercise is based on the previously published TEHD spherical shell convection experiment given by Travnikov et al. [13]. To ensure reliable solutions for the FVM solver, the PSM and FEM serve as benchmark solutions. The choice to extend the study by Travnikov refers to the complexity of the interactions of the underlying physical processes, such as spherical shell rotation, electric forcing, and dielectric heating. The present study describes the implemented equations and commonly established modelling approaches to characterise rotating TEHD convection in a spherical shell. The parametric study by Travnikov et al. [13] provides three basic flow regimes that are steady, axisymmetric, and equatorial symmetric, avoiding a spatial and temporal averaging of solutions providing a well-suited benchmark exercise for different numerical codes. This study and the custom-developed FVM solver intend to contribute towards the search for efficient, high-accuracy methods to solve TEHD-related convection problems.

2. Model formulation

This section deals with the problem geometry and the general form of the governing equations to solve the evolving TEHD convection in the spherical shell. This is followed by the choice of selected parameters, the numerical input, and the diagnostics to compare the different solvers.

2.1. **Problem geometry.** We consider a rotating TEHD convection of a Boussinesq dielectric fluid confined in a spherical shell between the inner radius, R_1, and outer radius, R_2, providing a radius ratio, η, and a shell thickness of $L = R_2 - R_1$ defined as the reference length. Spherical rotation is provided by a constant angular velocity, Ω, around the z-axis given by $(0, 0, \Omega)$. The spherical shells' temperatures are maintained to mimic a planet's atmosphere, with a heated equatorial region and cooled poles. The inner shell's temperature is defined by

$$T_{in}(\theta) = \left(\frac{T_1 + T_2}{2}\right) + \left(\frac{T_1 - T_2}{2}\right) \sin^n(\theta) \tag{1}$$

and the outer shell's temperature by

$$T_{out}(\theta) = T_2 + \left(\frac{T_1 - T_2}{2}\right) \frac{\cosh(a_{th}\cos(\theta)) - \cosh(a_{th})}{1 - \cosh(a_{th})} \tag{2}$$

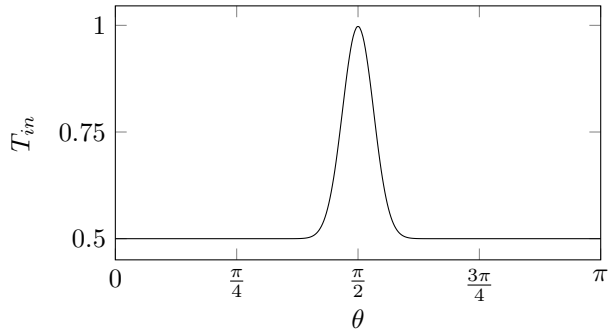

(a) Inner sphere

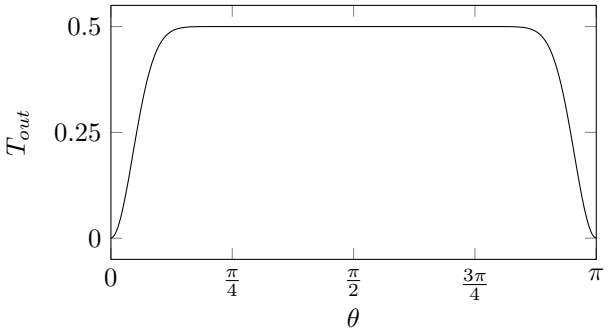

(b) Outer sphere

Figure 1. Temperature boundary conditions

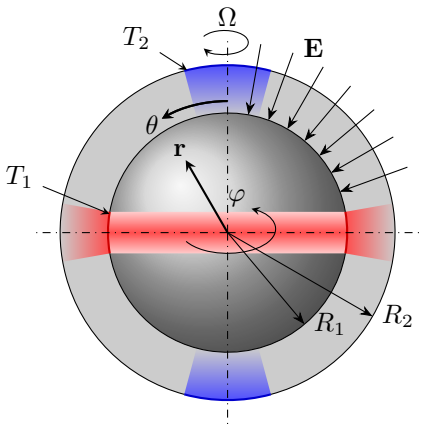

Figure 2. Schematic of the numerical model with boundary conditions

where θ is the inclination angle, T_1 the temperature at the equator, T_2 the temperature at each pole, providing a temperature difference $\Delta T = T_1 - T_2$ with $T_1 > T_2$. [1] The variables n and a_{th} are used for a planetary atmospheric-like boundary condition equal to 100 and 50, respectively. Velocity boundary conditions are no-slip at all walls and are impermeable. The temperature variation of T_{in} and T_{out} over the inner and outer shell are plotted in Figure 1(a) and 1(b), respectively. To induce TEHD convection, an alternating electric potential, $V(t)$, is applied at R_1, while R_2 is grounded. All boundary conditions are given in a schematic representation in Figure 2.

[1]The temperature difference, ΔT, is defined by the difference in temperature given at the equator and poles. This definition differs from the one of Travnikov et al. [13] given by $(T_1 - T_2)/2$ and is also reflected in the Rayleigh number, see eq.(22).

2.2. **Governing equations.** Exposing a dielectric fluid to an electric field creates a volumetric body force that is derived from the Kortweg-Helmholtz force density, written as

$$\mathbf{f}_E = \rho_e \mathbf{E} + \nabla \left[\rho \left(\frac{\partial \epsilon}{\partial \rho} \right)_T \frac{\mathbf{E}^2}{2} \right] - \frac{1}{2} \mathbf{E}^2 \nabla \epsilon \tag{3}$$

where ρ_e is the electric charge density, $\mathbf{E}$ the electric field, ρ the fluid's density and ϵ the electric permittivity. A full derivation of $\mathbf{f}_E$ is given by Landau et al. [33]. The first term on the right-hand side of eq.(3) is known as the Coulomb force or electrophoretic force. In the special case of static electric or low-frequency electric fields, the change in ρ_e may be greater than in ϵ, and the Coulomb force will dominate the flow. Suppose the electric field's frequency, f, is larger than the viscous timescale, τ_ν, the fluid is unable to respond to changes in $\mathbf{E}$ and the Coulomb force has no effect as long as $f >> \tau_e^{-1}$, where τ_e is the charge relaxation time defined by ϵ/σ_e with σ_e being the electric conductivity of the dielectric fluid [7,34,35]. For high-frequency electric fields, the Coulomb force may be neglected. Hence, the second and third force terms on the right-hand side of eq.(3) become dominant, as both owe a static component with $|\mathbf{E}|^2$. With an incompressible consideration and no mobile boundaries, the second term, the electrostrictive force, will have no influence on fluid motion and can be lumped into the pressure and treated as an electrostatic pressure term similar to the static head. The remaining term is the dielectrophoretic force (DEP) density, written as

$$\mathbf{f}_{DEP} = -\frac{1}{2} \mathbf{E}^2 \nabla \epsilon \left(T \right) \tag{4}$$

which owes a temperature dependence on electrical permittivity. Non-isothermal perturbation in the electric permittivity and in the presence of a high-frequency electric field can induce a thermally driven buoyant flow [34, 36, 37].

With the above problem definition, we consider an incompressible, Newtonian dielectric fluid free of electric charges. The continuity, momentum and energy equations read

$$\nabla \cdot \mathbf{u} = 0 \tag{5}$$

$$\frac{\partial \mathbf{u}}{\partial t} + (\mathbf{u} \cdot \nabla)\mathbf{u} = -\frac{1}{\rho_0} \nabla p + \nu \nabla^2 \mathbf{u} + \frac{1}{\rho_0} \mathbf{f}_i \tag{6}$$

$$\frac{\partial T}{\partial t} + (\mathbf{u} \cdot \nabla) T = \kappa \nabla^2 T + H_E \tag{7}$$

where $\mathbf{u}$ is the velocity, t the time, ρ_0 the density at reference temperature T_0, p the pressure, ν the kinematic viscosity, T the temperature, κ the thermal diffusivity and $\mathbf{f}_i$ represents any additional force density acting on the fluid. The parameter H_E is written as

$$H_E = \frac{2\pi f \epsilon_0 \epsilon_r h_{diss}}{\rho_0 c_p} |\mathbf{E}|^2 \tag{8}$$

and known as the dielectric heating parameter, where f is the frequency of the alternating electric field, ϵ_0 the permittivity of free space, ϵ_r the relative permittivity, h_{diss} the dielectric loss factor, also known as $\tan\delta$ counting for dielectric losses [13] and c_p the heat capacity. Those equations are derived from the work of Travnikov et al. [13]. Successful implementation and validation for the momentum equation are given by [6,15] together with energy equation and the additional dielectric heating source term by [5,38]. The set of these equations are adapted for the OpenFOAM ecosystem in the present work.

In the past decades, dielectric losses resulting in dielectric heating have been neglected, especially for small AC frequencies [37]. However, highly polar fluids may cause significant dielectric heating influencing the thermal flow, which can be accounted for by H_E. Maxwell's equations govern the alternating electric field written as $V(t) = \sqrt{2} V_0 \sin(2\pi f t)$ and counts for the temperature differences in the electric permittivity. For a high-frequency electric field compared to the viscous timescale, $\tau_\nu = L^2/\nu$, only the time-averaged DEP force can induce the convective motion of the fluid. This assumption is valid according to Turnball [39] and Stiles [37]. Hence, the Maxwell's equations reduce to Gauss's law, which reads

$$\nabla \cdot \left[\epsilon \left(T \right) \mathbf{E} \right] = 0, \quad \text{with} \quad \mathbf{E} = -\nabla V_0 \tag{9}$$

where ϕ is the electric potential.

The temperature-dependent fluid properties are governed by the Boussinesq-Oberbeck approximation, stating that all parameters are held constant with T except for the fluid's density in the centrifugal buoyancy term and the electric permittivity where buoyancy-driven flow may occur [36]. One can now express the thermal variations in density as

$$\rho(T) = \rho_0 (1 - \alpha (T - T_0)) \tag{10}$$

where α is the thermal expansion coefficient. An equivalent equation of temperature deviation in $\epsilon(T)$ is expressed by

$$\epsilon(T) = \epsilon_0\epsilon_r(1 - e(T - T_0)) \tag{11}$$

where e is the thermal variation coefficient of the electric permittivity. The eq.(10) and eq.(11) are linearly dependent on temperature and valid as long as the imposed temperature difference is small, see [13, 18, 21, 40].

As outlined above, the volumetric forces acting on the fluid can now be defined in a non-isothermal rotating dielectric fluid in the presence of the effective electric potential, V_0. Considering a Boussinesq dielectric fluid, the DEP force in eq.(4) can be rewritten as

$$\mathbf{f}_{DEP} = \frac{\epsilon_0\epsilon_r e}{2}\left(-\nabla V_0\right)^2 \nabla T. \tag{12}$$

with the electrohydrodynamic Boussineseq eq. given in eq.(11). Spherical shell rotation is governed by the rotating framework of reference and expressed by the Coriolis force density

$$\mathbf{f}_{Co} = -2\rho_0\, \boldsymbol{\Omega} \times \mathbf{u} \tag{13}$$

and centrifugal force density,

$$\mathbf{f}_{Cf} = -\rho_0\, \boldsymbol{\Omega} \times (\boldsymbol{\Omega} \times \mathbf{r}) \tag{14}$$

where $\mathbf{r}$ is the radial vector from the axis of rotation. Since the imposed rotation Ω is time invariant $\partial\Omega/\partial t = 0$, the Euler force is absent. For rapid rotating systems, the centrifugal force can cause centrifugal Rayleigh-Bénard convection in a non-isothermal fluid, see [41, 42]. Density variations in the centrifugal force density may become important where higher dense fluid is displaced away for the axis of rotation, leading to an additional acceleration term given by

$$\mathbf{f}_{Cb} = \rho_0\, \alpha\Delta T\, [\boldsymbol{\Omega} \times (\boldsymbol{\Omega} \times \mathbf{r})] \tag{15}$$

known as the centrifugal buoyancy force density [12, 13, 21].

The pressure, p, in the momentum eq.(6) can now be modified and includes the prior defined electrostrictive force lumped into the pressure term as

$$P = p - \frac{1}{2}\left(\frac{\partial\epsilon}{\partial\rho}\right)_T \mathbf{E}^2 \tag{16}$$

where the centrifugal force density in eq.(14) can either be left as a force density in the momentum equation or included in the pressure term by $1/2\,\Omega^2 r^2$ as suggested by [43]. For the sake of simplicity and the way how the finite volume solver is implemented, the centrifugal force density remains in the momentum equation.

The governing equations, eq.(5)-(7) and eq.(9) can be formulated in dimensionless form using an appropriate scaling. To be consistent with Travnikov et al. [13], we use the thermal timescale, which is given by the characteristic length of the system, $L = R_2 - R_1$, and the thermal diffusivity, κ and written as $\tau_\kappa = L^2/\kappa$. Hence, the following non-dimensional variables are obtained

$$\mathbf{u}^* = \mathbf{u}\frac{L}{\kappa}, \quad t^* = t\,\frac{\kappa}{L^2}, \quad \nabla^* = L\nabla, \quad , P^* = P\frac{L^2}{\rho_0\kappa^2}, \quad T^* = \frac{T - T_0}{\Delta T}, \quad \mathbf{E}^* = \mathbf{E}\frac{L}{V_0} \tag{17}$$

and one can formulate the continuity, momentum, energy and Gauss equation with the force densities given in eq.(12) -(15) and the modified pressure in eq.(16) in non-dimensional form[2]

$$\nabla \cdot \mathbf{u} = 0 \tag{18}$$

$$\begin{aligned}\frac{\partial\mathbf{u}}{\partial t} + (\mathbf{u}\cdot\nabla)\mathbf{u} = &-\nabla P + Pr\,\nabla^2\mathbf{u} \\ &- Pr\sqrt{Ta}\,\mathbf{e}_z \times \mathbf{u} \\ &- \frac{1}{4}Pr^2\,Ta\,r\,\mathbf{s} \\ &+ \frac{1}{4}Pr^2\,Ta\,(\alpha\Delta T)Tr\,\mathbf{s} \\ &+ Pr\,Ra_E|\mathbf{E}|^2\nabla T\end{aligned} \tag{19}$$

$$\frac{\partial T}{\partial t} + (\mathbf{u}\cdot\nabla)T = \nabla^2 T + \frac{Ra_E}{Ra_T}|\mathbf{E}|^2 \tag{20}$$

$$\nabla\cdot\mathbf{E} - e\Delta T\,\nabla\cdot(T\,\mathbf{E}) = 0, \quad \text{with} \quad \mathbf{E} = -\nabla\vartheta \tag{21}$$

[2]Note that for the sake of clarity the asterisk, which denotes the dimensionless variables above are revoked to avoid overloading of symbols. The following equations are all dimensionless:

where ϑ is the non-dimensional electric potential, $\mathbf{s}$ is defined by $-(\sin\theta\,\mathbf{e}_r + \cos\theta\,\mathbf{e}_\theta)$ with the unit norm vectors $\mathbf{e}_r$, $\mathbf{e}_\theta$ and $\mathbf{e}_z$ in radial, meridional and vertical direction, respectively. The defined set of equations is given in the Cartesian coordinate system and is used for the FVM and FEM method of solution. In contrast, the Polar coordinate system is used for the PSM solution method with r the radius, φ the azimuth angle and θ the inclination angle, see Section 3.3. The non-dimensional equations are governed by the Prandtl number, Pr, the Taylor number, Ta and the Rayleigh numbers, Ra_E, and Ra_T, defined by

$$Pr = \frac{\nu}{\kappa}, \quad Ta = \frac{4\Omega^2 L^4}{\nu^2}, \quad Ra_E = \frac{\epsilon_0 \epsilon_r e \Delta T V_0^2}{2\rho_0 \nu \kappa}$$
$$Ra_T = \frac{c_p e \Delta T^2}{4\nu\pi f h_{diss}} \tag{22}$$

and provide an indication of the relative importance of buoyant forcing to Coriolis forcing and thermal forcing in rotating TEHD convection.[3]

Table 1. Parameter space and regimes after Travnikov et al. [13].

Regime	Ta	Ra_E	Ra_T
I	10^3	0	-
II	$1.5 \cdot 10^4$	$1.9182 \cdot 10^4$	$2.0213 \cdot 10^5$
III	10^3	10^5	$2.0213 \cdot 10^5$

2.3. **Parameter choice, numerical input and evaluation.** To compare the methods of solutions with one another, the choice was made to use the basic flow of three distinct regimes occurring in a spherical shell geometry with aspect ratio $\eta = 0.7$ defined by Travnikov et al. [13]. The so-called basic flow is steady-state, symmetric around the rotation axis and symmetric to the equatorial plane. Hence, the uncertainty can be evaluated directly rather than using spatial and temporal averaging over a period of conductive time scales. While only three basic flow regimes exist, only three different parameters were selected. These regimes occur as a result of the competition between buoyancy, Coriolis, and centrifugal forces. The forcing parameters of the three regimes are given in Table 1 and investigate a rotating dominated flow regime in regime (I), a combined regime of almost equivalent forcing strength in thermal and rotational forcing in regime (II) and a thermally forced dominated regime with small rotational forcing in regime (III). The selected forcing parameters are chosen in a much larger parametric study; see [13].

The system is solved in non-dimensional form by using the forcing parameters introduced in eq.(22) with the values given in Table 1 for each regime. Hence, the boundary conditions read in the non-dimensional form as

$$\begin{cases} \mathbf{u} = 0, \quad T = T_{in}(\theta), \quad \vartheta = 1, \quad \text{at} \quad r = \dfrac{\eta}{1-\eta} \\ \mathbf{u} = 0, \quad T = T_{out}(\theta), \quad \vartheta = 0, \quad \text{at} \quad r = \dfrac{1}{1-\eta} \end{cases} \tag{23}$$

where T_1 and T_2 in eq.(2.1) and eq.(2.1) have the value 1 and 0, respectively. As we benchmark the methods of solution with the extended study of Travnikov et al. [13], the values for the radius ratio and the fluid properties are kept fixed to $Pr = 10.43$, $\alpha\Delta T = 0.0361$ and $e\Delta T = 0.0241$ to limit the parameter space and explorer only the three basic flow regimes. Quantities such as $\alpha\Delta T$ and $e\Delta T$ are non-dimensional parameters that can be denoted as γ_α and γ_e and are known as the volumetric expansion parameter [19], and the thermoelectric parameter, respectively. One has to note that the onset of convection is dependent on these parameters, see [1, 5–7].

The numerical evaluation and benchmark of the methods of solutions are compared by local, velocity and temperature profiles at the equator and pole planes of the system and by the heat flux across the inner and outer shell given by

$$Q = \int \frac{\partial T}{\partial r} dS \tag{24}$$

[3]The definition of the Rayleigh number differs by a factor of two compared to Travnikov et al. [13] and refers to the different definition of the temperature difference which was mentioned in Section 2.1 earlier. The choice was made to use the current definition, which clearly implements the correct governing equations in the FVM solver.

where S is the inner or outer spherical shell surface, respectively. An indication of the intensity of the overall heat flux across the shell's surfaces can be given by the Nusselt number written as

$$Nu = \frac{Q_{conv} + Q_{cond}}{Q_{cond}} \tag{25}$$

where Q_{conv} and Q_{cond} are the convective and conductive heat flux, respectively. The conductive heat flux is defined after Travnikov et al. [13] and only counts for the conductive transport in the absence of the electric voltage where dielectric heating is not present.

3. Numerical methods of solution and resolution requirements

In the following section, the numerical methods of solution are introduced. This concerns the numerical principle of the finite volume, finite element, and pseudo-spectral methods with their discretisation schemes and the solvers used.

3.1. **Finite volume method.** The finite volume method used is based on the open-source CFD Toolbox for engineering and multiphysics problems named OpenFOAM. The code is open-source, written in C++ and supports parallelisation using MPI libraries. The finite volume method discretises the fluid region in small volumes, known as cells. All applied forces on the fluid volume result in a flux passing the cell faces, obeying the continuity equation. Gradients are locally built using the finite area of a cell and solved using the OpenFOAM® in-house named algorithm PIMPLE. The name is a combination of two algorithms, namely PISO and SIMPLE. Both algorithms are able to solve pressure and velocity-coupled equations. While the SIMPLE algorithm is a steady-state solution only solver solving iteratively until a predefined residual is achieved where the solution converges, the PISO algorithm is used for transient solutions where the CFL number remains below 1 to ensure an accurate solution. Combining both algorithms in terms of using a SIMPLE loop for the overall correction with a nested PISO loop for transient solutions, the solver is able to solve transient problems with larger CFL values than 1, which increases the overall computational performance significantly. The working principle is based on the PISO loop that is repeated by the SIMPLE loop until the residual is met. The pressure-velocity coupling is then solved by the algorithm and includes all quantities lumped in the pressure term, e.g., $p = F(\mathbf{u})$ [44].

The pressure matrix results from the fluxes of the volumetric forces and is solved implicitly. For solving the energy and Gauss equation, a segregated step is used to count for all forces acting on the control volume. The solution is given when the residual is below a predefined threshold at a given time step before the loop restarts. A common value to ensure a converged solution is found for residuals below $1e-4$ and is usually reached between two to five PIMPLE iterations. The segregated step of solving the divergence of the electrostatic Gauss equation is done implicitly to be able to find solutions when sharp edges or geometries are present, which provides better numerical convergence than using an explicit scheme. All other equations are solved with a corrector loop starting with the Gauss matrix, which processes simultaneously the electric force field. Thereafter, the pressure matrix is solved, including two non-orthogonal iterations to ensure convergence, as the used hexahedron mesh has slightly skewed cells when geometries with curvatures are used. In the final step, the temperature matrix is solved by including the dielectric heat generation caused by the alternating electric field.

The numerical model is discretised such that all operations, like differentiation or integration and discrete methods, need to be applied. As no turbulence modelling is used, discretisation is conservative. A second-order scheme for divergence and Laplace operation with a central difference scheme is used, given by

$$\Phi_e = \frac{\Phi_E + \Phi_W}{2} \tag{26}$$

which is applied due to their low numerical dissipation properties [44]. The trade-off is dispersion errors, which require an enhanced mesh and more iteration to convergence. The mesh is structured and composed of hexahedron cells to guarantee maximum orthogonality. The least squares scheme is chosen for gradient operations. In OpenFOAM the least-squares gradient calculates the gradient using all cell faces geometric instead of cell centroids. This enhanced the robustness of the gradient calculation. The time discretisation is performed using a Crank-Nicholson (CN) scheme. This ensures small numerical dissipation while maintaining numerical stability. The simulations are processed using CN's blend value 0.9. After discretising, all the matrices are built and solved implicitly to ensure faster calculation and more robustness. Symmetrical matrices like the pressure and electrical field matrices use a Geometric Adaptive Multigrid (GAMG) solver with a V-cycle [30]. This solver coarsens the mesh, solving fewer degrees of

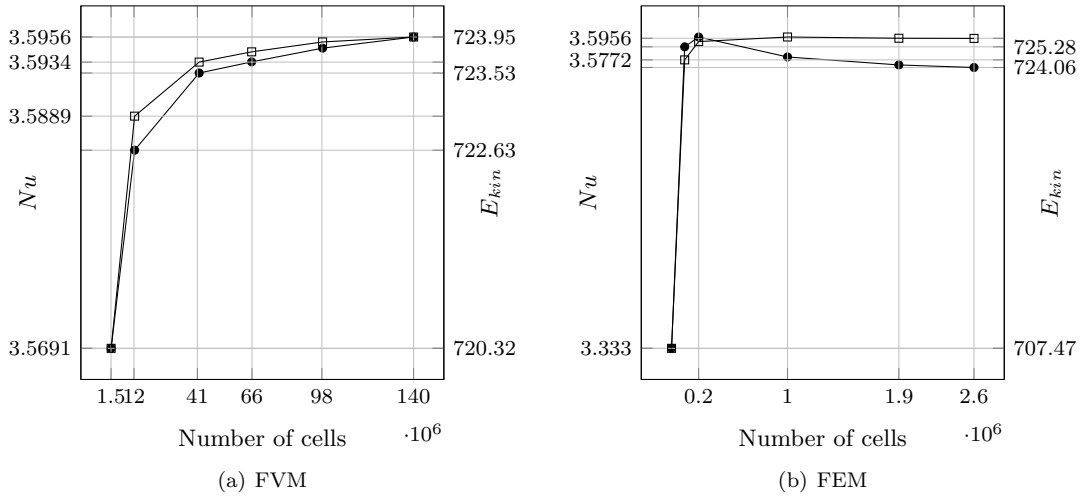

(a) FVM (b) FEM

Figure 3. The Nusselt number, Nu (—▫—) and volumetric averaged kinetic energy E_{kin} (—•—) plotted versus the number of elements for the grid independence of the FVM and FEM technique at Rayleigh number $Ra_E = 2 \cdot 10^5$ and Taylor number $Ta = 10^3$

freedom, and then interpolates again on all the degrees of freedom for the full grid size. Hence, corrector cycles are usual practices to enforce convergence. For non-symmetric matrices like the temperature matrix, a bi-conjugate gradient solver is used.

Figure 3 depicts the grid independence test via the Nusselt number and the kinetic energy for the largest forcing parameter for the FVM and FEM in (a) and (b), respectively. Reliable solutions are found for grid sizes above 41 million cells and 1.9 for the FVM and FEM, respectively.

3.2. **Finite element method.** The numerical model is solved with the boundary conditions given in eq.(23) by a finite element technique developed by COMSOL [45]. The FEM was benchmarked for thermal convection by using the de Vahl Davis [46] benchmark solution for natural convection in an air-filled cavity. The benchmark provided a qualitative good agreement with a difference in Nu of less than 0.76%. The complete benchmark solution is found in Table 3 in [47].

A tetrahedral mesh was generated and showed convergence of reliable solutions for a grid size of about half a million elements. To provide a finer resolution of the temperature and velocity, a total of 1,837,349 elements were chosen. The unstructured mesh provided more flexibility about the distribution of elements to compensate for equal element size in the domain. On the outer shell, 200 elements are in azimuthal and meridional direction, whereas in the inner shell, the number of elements is scaled with 200η. The volume could, therefore, be meshed with relatively uniform-sized tetrahedral elements attached to the boundary elements by using two boundary layers with a stretching factor of 1.2 towards the inner and outer shells.

The numerical model was solved in two solution stages. The first stage solved the Gauss equation and the conductive base state. The solution was then used as initial values for the time evolution of the transient solvers. A quadratic discretisation is used to solve the static Maxwell equations. For temperature, a quadratic Lagrange and a second-order element discretisation are used for pressure and velocity. The pressure and velocity are solved by the Generalized Minimum Residual (GMRES) iterative solver, which uses a smoothed aggregation algebraic multigrid with an F-cycle. The temperature equation is also solved by a GMRES using a geometric multigrid solver with a V-cycle. The static Maxwell equations are solved by a segregated step iteratively by a conjugate gradient solver. All solvers run simultaneously, such that the temperature variations are coupled with the non-isothermal flow and the Gauss equation. Consistent stabilisation is provided by a streamline and crosswind diffusion. The time is discretised by a Backward Differentiation Formula (BDF) method, also known as backward Euler, which is an implicit solver of second-order accuracy. A free time stepping is used to take larger or smaller time steps as required to satisfy the specified tolerances.

3.3. **Pseudo spectral method.** The pseudo-spectral method developed by Hollerbach [22] is a Fortran-based code for simulating geophysical flows. The code runs on a single core and is, to the best of the authors' knowledge, not yet parallelised. The PSM code uses the spherical coordinate system (r, θ, φ) as outlined already above in section 2.2 where the Cartesian unit norm vectors relate to the spherical unit

Table 2. Mesh structure and computational effort normalised for convergence and CPU time.

	FVM (OpenFOAM®)	FEM	PSM
Element type	Structured hexahedron	Unstructured tetrahedral	Points
Points in $r - \theta - \varphi$	$120 \times 960 \times 960$	Mixed	$50 \times 420 \times -$
Approx normalized convergence time	12h	103h	72h
Approx normalized convergence CPU time	4608h	2060h	72h

norm vectors by a rotation matrix as follows

$$\begin{bmatrix} \mathbf{e}_x \\ \mathbf{e}_y \\ \mathbf{e}_z \end{bmatrix} = \begin{bmatrix} \sin\theta\cos\varphi & \cos\theta\cos\varphi & -\sin\varphi \\ \sin\theta\sin\varphi & \cos\theta\sin\varphi & \cos\varphi \\ \cos\theta & -\sin\theta & 0 \end{bmatrix} \begin{bmatrix} \mathbf{e}_r \\ \mathbf{e}_\theta \\ \mathbf{e}_\varphi \end{bmatrix}. \tag{27}$$

The velocity is decomposed into poloidal, Φ, and toroidal, Ψ, contributions given by

$$\mathbf{u} = \nabla \times \nabla \times (\Phi\,\mathbf{e}_r) + \nabla \times (\Psi\,\mathbf{e}_r). \tag{28}$$

which has the advantage that the continuity is automatically obeyed. As outlined in section 2.3 the specified regimes are quasi-stationary and axisymmetric and hence depend only on r and θ where $\partial/\partial\varphi = 0$. Zero points are therefore defined in the direction of φ. The equations for Φ and Ψ are obtained by applying the operators $\nabla \times \nabla\times$ and $\nabla\times$, respectively, which eliminates the pressure of the systems, and one arrives at

$$\begin{aligned} &\frac{1}{r^2}\nabla_s^2\left(\frac{\partial^2}{\partial r^2} + \frac{\nabla_s^2}{r^2}\right)\left[\frac{\partial}{\partial t} - \left(\frac{\partial^2}{\partial r^2} + \frac{\nabla_s^2}{r^2}\right)\right]\Phi(t,r,\theta) \\ &= (\nabla \times \nabla \times \mathbf{G})_r \end{aligned} \tag{29}$$

$$-\frac{1}{r^2}\nabla_s^2\left[\frac{\partial}{\partial t} - \left(\frac{\partial^2}{\partial r^2} + \frac{\nabla_s^2}{r^2}\right)\right]\Psi(t,r,\theta) = (\nabla \times \mathbf{G})_r, \tag{30}$$

where $\mathbf{G}$ are the lumped forcing parameters given by

$$\begin{aligned} \mathbf{G} = &- Pr\; Ra_E T\; \nabla[\nabla\vartheta_0(r) + \nabla\vartheta\,(r,\theta)]^2 \\ &- Pr^2\,\sqrt{Ta}\,\mathbf{e_z} \times \mathbf{u} \\ &+ \frac{1}{4} Pr^2\, Ta\, \gamma_\alpha\, Tr \sin\theta\, \mathbf{s} \end{aligned} \tag{31}$$

suggesting the following vector operator

$$\nabla_{\mathrm{s}}^2 \cdot = \frac{1}{\sin\theta}\frac{\partial}{\partial\theta}\left(\sin\theta\frac{\partial\cdot}{\partial\theta}\right) \tag{32}$$

The velocity boundary conditions in eq.(23) read for the PSM

$$\begin{cases} \Psi = 0, \quad \Phi = 0, \quad \dfrac{\partial\Phi}{\partial r} = 0, \quad \text{at} \quad r = \dfrac{\eta}{1-\eta} \\ \Psi = 0, \quad \Phi = 0, \quad \dfrac{\partial\Phi}{\partial r} = 0, \quad \text{at} \quad r = \dfrac{1}{1-\eta} \end{cases} \tag{33}$$

and are in no-slip conditions. Each scalar function of poloidal and toroidal velocity can be represented in terms of Chebyshev polynomials and spherical harmonics according to

$$\Phi \;=\; \sum_{\ell=1}^{LU} \tilde{g}_\ell(r,t) P_\ell^0(\cos\theta = \sum_{\ell=1}^{LU}\sum_{k=1}^{KU+4} g_{k\ell}(t) T_{k-1}(x) P_\ell^0(\cos\theta), \tag{34}$$

$$\Psi \;=\; \sum_{\ell=1}^{LU} \tilde{f}_{c\ell}(r,t) P_\ell^0(\cos\theta) = \sum_{\ell=1}^{LU}\sum_{k=1}^{KU+2} (f_{ck\ell}(t)) T_{k-1}(x) P_\ell^0(\cos\theta), \tag{35}$$

A similar expression can be formulated for the temperature by

$$T = \sum_{\ell=0}^{LT} \tilde{t}_{c\ell}(r,t) P_\ell^0(\cos\theta) = \sum_{\ell=0}^{LT} \sum_{k=1}^{KT+2} t_{ck\ell}(t) T_{k-1}(x) P_\ell^0(\cos\theta), \tag{36}$$

and analogous to the electric potential for solving the Gauss equation by

$$\vartheta = \sum_{\ell=0}^{LP} \tilde{p}_{c\ell}(r,t) P_\ell^0(\cos\theta) = \sum_{\ell=0}^{LP} \sum_{k=1}^{KP+2} p_{ck\ell}(t) T_{k-1}(x) P_\ell^0(\cos\theta). \tag{37}$$

The mapping is performed by

$$r(x) = \frac{1}{2}\Big[x + \frac{1+\eta}{1-\eta}\Big] \tag{38}$$

and used to transform Chebyshev polynomials defined in the interval $[-1, 1]$ into the domain $\mathrm{r} \in [\eta/(1-\eta), 1/(1-\eta]$. The truncation order for the Chebyshev polynomials is KU, KT, KP for the poloidal and toroidal potentials, the temperature and electrical potential, respectively. The corresponding truncation orders for the Legendre polynomials are given by LU, LT, LP. Note that the collocation points were found analytically as roots of the Chebyshev polynomial $\mathrm{T_{KN}(x)}$ in the radial direction

$$x_j = -\cos\left[\frac{(2j-1)\pi}{2KN}\right] \tag{39}$$

and numerically as roots of the Legendre polynomial $\mathrm{P_{LN}}(\cos\theta)$ in the latitudinal one. The 3/2 rule is used as a connection between the truncation order and a number of the collocation points

$$KN = 3/2 \max(KU, KT), \qquad LN = 3/2 \max(LU, LT). \tag{40}$$

Time-dependent spectral coefficients are calculated due to the predictor-corrector method. To provide reliable solutions for temperature and velocity, the Nusselt number and critical Rayleigh number, $\mathrm{Ra_{Ec}}$, and the frequency of the perturbation as fixed Δt are used as control parameters to perform the convergence analysis. The time step varied between 10^{-4} and 10^{-5}. To fully resolve the velocity field according to the work of Travnikov et al. [13], 20 Chebyshev polynomials and up to 160 Legendre polynomials were required. With the specific boundary conditions for the temperature, a maximum of 30 Chebyshev polynomials and up to 280 Legendre polynomials were necessary to calculate the temperature field accurately. For ensuring reliable results, sufficient points had to be selected for computation. With the 3/2 rule named in eq.(40) results in at least 45 points in the radial direction and 420 points in the meridional direction. A slightly larger number of points is used for the radial direction and summarised in Table 2. The azimuthal direction has no points resolved since the calculations are 2D for the PSM.

3.4. **Spatial discretion and time of solution.** While the discretisation between the methods of solution varies and is not the same, one has to pay special attention to the numerical method used to solve the transport equations. As the PSM and FEM methods use nodal points in the fluid domain, the solution procedure uses polynomials and shape functions, respectively. This is different from the FVM methods that used fluxes across cell faces, and calculates from those fluxes balance the information at the cell centroid. This method has the limitation of having pointwise information from cell to cell instead of a smooth transition. PSM and FEM can therefore reach accurate solutions with comparable fewer points when discretising the mesh as FVM. Also, the pseudo-spectral method, for example, uses 50 Chebyshev polynomials per point in the radial direction for the velocity, resulting in 1000 degrees of freedom for the PSM method. The computational effort to solve all equations is reflected in the solution time. Temporal convergence of the numerical models is ensured by running the simulations for at least 10 thermal time scales. A quasi-stationary state was given after a settling period of about two thermal time scales. An overview of all three methods is given in Table 2 with the respective mesh indicating a much faster solution for the PSM and FEM compared to the FVM.

Comparing all methods suggests a disadvantage for the OpenFOAM® solver in computational cost when compared to the other two methods. From a first point of view, the simulation time of the PSM method shows a significant advantage; however, it is performed in 2D, not 3D. While the PSM method is capable of solving in 3D, it is not required here as the cases considered here can be computed in 2D, resulting in less computational time compared to the 3D cases of FVM and FEM. In addition, the PSM method used is not yet parallelised and requires a large computational time when processing on a single core, see [13]. The computational advantage of the PSM is limited to more complex geometries and asymmetric properties when compared to the other methods. One can now conclude that the FVM has a broader possibility of applications compared to the PSM, even when comparing the non-trivial

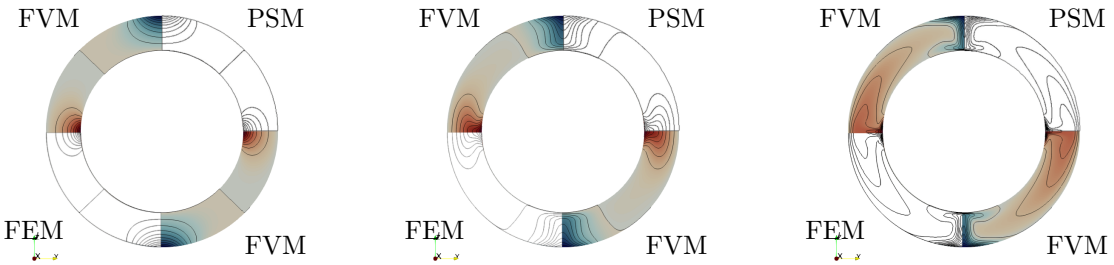

(a) $Ta = 10^3$ $Ra_E = 0$ (b) $Ta = 1.5 \cdot 10^4$ $Ra_E = 19182$ (c) $Ta = 10^3$ $Ra_E = 1 \cdot 10^5$

Figure 4. Temperature contour plot with range (0,0.05,1) of the north-south plane of the spherical shell. The panels represent the regimes (I-III) from left to right, respectively. Each panel consists of a quarter of the individual solution method PSM and FEM, while the solution of FVM is given twice to compare the contours of each solution.

implementation of parallel computing of the PSM. Comparing the commercial FEM solver with FVM requires half of the computational time of the FVM. However, commercial solvers usually require a license, which may also limit the parallel scalability depending on the acquired license. The emerging field of TEHD requires flexibility for both the development and computation with an open-source environment like OpenFOAM® provides.

4. Results and discussion

In this section, we present the results of the three different methods of solution. The results are given after the settling period, when the system had equilibrated to a quasi-steady state for each regime (I-III) representing the basic flow. The three regimes of the basic flow are evaluated by the temperature distribution, the convective flow, and the heat transfer.

4.1. **Temperature fields.** Figure 4 presents a north-south plane of the spherical shell's temperature distribution of the basic flow. To compare the individual methods of solution, the temperature plane is composed of the PSM and FEM solution and enclosed by the solution of the FVM method to compare the fitting of the contours.

The first regime (I) investigates the rotating regime without electric forcing $Ra_E = 0$ and a relatively small Taylor number of $Ta = 10^3$. The observed temperature field is similar to the conductive result. However, the contours tend to bend inwards at the equator and outwards at the poles of the spherical shell, suggesting convection that only occurs due to centrifugal buoyancy. Hence, the centrifugal force is the only force responsible for the formation of the basic flow. The basic flow's thermal structure is preserved for larger Taylor numbers and small electric Rayleigh numbers.

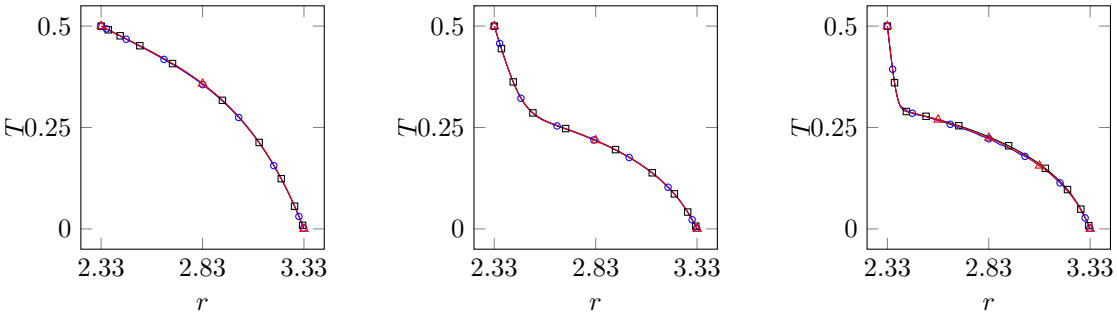

(a) $Ta = 10^3$ $Ra_E = 0$ (b) $Ta = 1.5 \cdot 10^4$ $Ra_E = 19182$ (c) $Ta = 10^3$ $Ra_E = 1 \cdot 10^5$

Figure 5. Radial temperature distribution at the North Pole ($\theta = 0$) for all basic flow regimes and methods of solution. FVM (—▫—), FEM (—○—) and PSM (—△—).

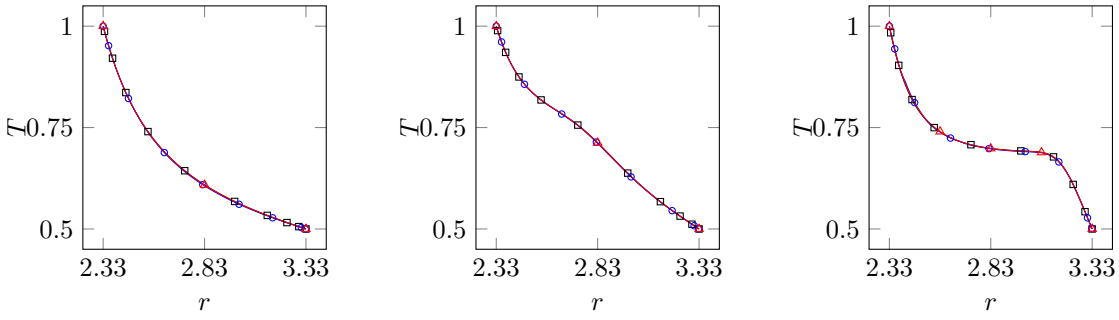

(a) $Ta = 10^3$ $Ra_E = 0$ (b) $Ta = 1.5 \cdot 10^4$ $Ra_E = 19182$ (c) $Ta = 10^3$ $Ra_E = 1 \cdot 10^5$

Figure 6. Radial temperature distribution at the equator ($\theta = \pi/2$) for all basic flow regimes and methods of solution. FVM (—▫—) and FEM (—○—) and PSM (—△—).

The second regime (II) in the middle panel is observed when Ra_E increases in strength. A new basic flow is observed, where the temperature contours tend to bend outwards, whereas the contours at the poles bend inwards. The change in the regime suggests a convective motion of fluid related to the radial electric forcing. The overall temperature distribution is mushroom-shaped at the equator, with a plume of cold fluid at the poles.

The last and third regime (III) is present when the electric Rayleigh number is large $Ra_E = \mathcal{O}\ (10^5)$ and the Taylor number is small $Ta = \mathcal{O}\ (10^3)$. The mushroom-shaped temperature field extends from the equatorial region towards the poles, suggesting strong convective motion due to the large Ra_E and small Ta.

While matching the thermal contours provides only a qualitative agreement, a quantitative comparison between the methods is given in Figure 5 and Figure 6. Both figures present the radial temperature distribution between the inner and outer shell at the North Pole and equator, respectively. For regime (I) a logarithmic decay of the temperature is observed between the inner and outer shell, suggesting a temperature distribution close to the onset of convection. The second regime (II) shows a logarithmic decrease and indicates a convective flow as thermal boundary layers, δ_T, tend to appear. These are more pronounced for the regime (III), where the thickness decreases. Comparing both panels in Figure 5 and Figure 6 with one another, no significant difference is found across the three solution methods providing a well-matched temperature profile.

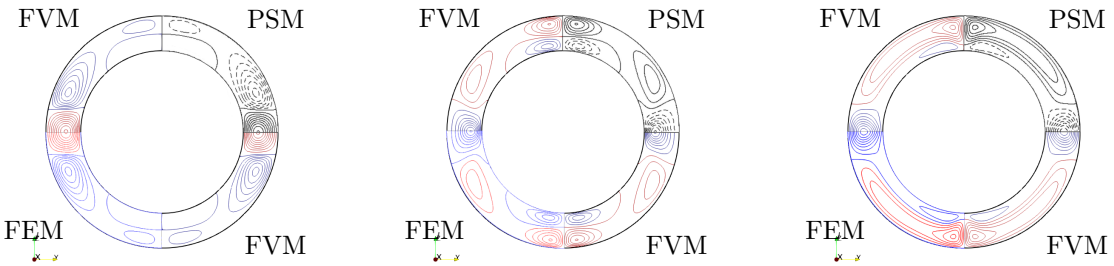

(a) $Ta = 10^3$ $Ra_E = 0$ (b) $Ta = 1.5 \cdot 10^4$ $Ra_E = 19182$ (c) $Ta = 10^3$ $Ra_E = 1 \cdot 10^5$

Figure 7. Azimuthal velocity, U_φ, a contour plot of the north-south plane of the spherical shell. The panels represent the regimes (I-III) from left to right, respectively. Each panel consists of a quarter of the individual solution method PSM and FEM, while the solution of FVM is given twice to compare the contours of each solution. The contour maximum and minimum values are in (a) +0.18 (0.02), -0.06 (0.01); (b) +20.0 (4.0), -40.0 (5.0); and (c) +50.0 (5.0), -80.0 (10.0), where the in-parenthesis values are the contour step

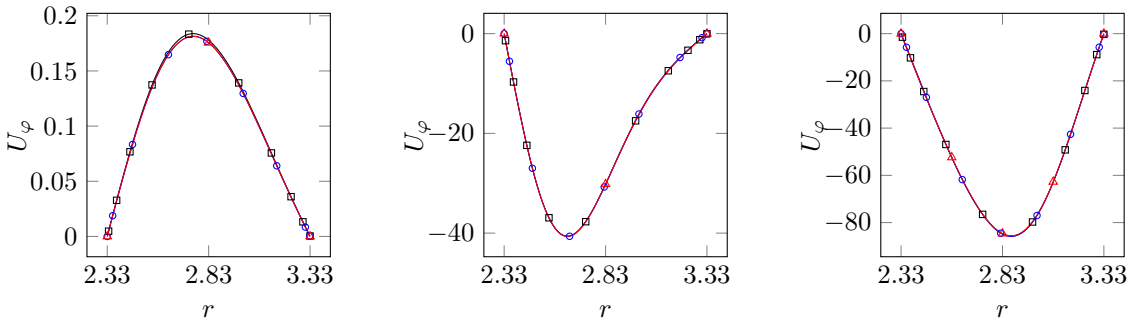

(a) $Ta = 10^3$ $Ra_E = 0$ (b) $Ta = 1.5 \cdot 10^4$ $Ra_E = 19182$ (c) $Ta = 10^3$ $Ra_E = 1 \cdot 10^5$

Figure 8. Azimuthal velocity at the equator ($\theta = \frac{\pi}{2}$) for all basic flow regimes and methods of solution. FVM (—▫—) and FEM (—○—) and PSM (—△—). One has to note that the velocity is zero due to the no-slip condition, as the system is in the rotating frame of reference.

4.2. **Convective flow.** After comparing the thermal distribution, the resulting convective flow is shown as contour plots in Figure 7 for all basic flow regimes.

In regime (I) the centrifugal force is responsible for the thermal distribution. The relatively small velocities are dominant at the equator, displaying colder, dense fluid towards the outer shell, bending the thermal isotherms inward. The azimuthal velocity component refers to the Coriolis force and has the largest positive value at the equator.

Regime (II) represents a convective regime. The fluid is heated in the equatorial region owing to radial and meridional components. The DEP force triggers the flow, where hotter fluid with larger electric permeability is displayed radially outwards towards the outer shell. The meridional component indicates a flow of hotter fluid moving polewards, cooling the fluid such as it descends towards the inner shell. The poleward flow deviates towards the east at the outer shell due to the Coriolis force in the upper part, while at the inner surface, the flow deviates towards the west. A second convective cell is observed at the pole and is caused by convective motion, attracting colder fluid towards the inner shell, where it moves towards the larger meridional cell, displacing towards a poleward transport to close the loop. The pole cell has an inclination, where the mechanism of this deviation is the same as that of the equatorial cell.

Table 3. Solution of Nusselt number, Nu, temperature, T, at the mid-gap and maximum value of the azimuthal velocity component, $|u_\varphi|_{max}$, with location of all basic flow regimes.

	Nu inner shell	Nu outer shell	T at $r = 2.833$ $\theta = 0$	T at $r = 2.833$ $\theta = \pi/2$	$\lvert u_\varphi \rvert_{max}$ at $\theta = \pi/2$
Regime I					
FVM	1.0005	1.0005	0.3580	0.6086	0.1838 at $r = 2.7535$
FEM	0.9889	0.9889	0.3557	0.6046	0.1814 at $r = 2.7515$
PSM	0.9880	0.9880	0.3580	0.6086	0.1813 at $r = 2.7583$
Regime II					
FVM	1.8172	3.1472	0.2271	0.6986	85.7140 at $r = 2.8746$
FEM	1.7957	3.1102	0.2221	0.6971	85.8694 at $r = 2.8829$
PSM	1.7963	3.1107	0.2124	0.6985	85.5834 at $r = 2.8758$
Regime III					
FVM	3.6358	10.5687	0.2185	0.7125	40.6130 at $r = 2.6403$
FEM	3.5961	10.4417	0.2165	0.7111	40.6670 at $r = 2.6428$
PSM	3.5978	10.4499	0.2182	0.7124	40.6336 at $r = 2.6433$

Regime (III) shows a strong radial flow that is deviated from the equator towards the poles. The fluid descends towards the inner shell at the pole and moves towards the equator. Hence, a large convective cell is present, filling the complete meridional plane. A similar convective flow is observed compared to the regime (II) where poleward flow is deviated towards the east while the flow at the inner shell deviates towards the west.

The contours for velocity compared to the different solution methods are well-matched and are in agreement with the temperature contours. However, a qualitative comparison of the azimuthal velocity at the equator reveals a small difference for the first regime, see Figure 8. The azimuthal velocity component of the regime (I) shows a marginal error when comparing FVM with the other two methods. However, the error is in the range of 1% or less and refers to the computational accuracy. For regimes with a larger Taylor and Rayleigh number of regimes (II) and (III) no notable difference is observed between the methods. The velocity shows kinematic boundary layers, δ_u, that are larger than the thermal boundary layers $\delta_T \ll \delta_u$ as seen in the temperature plots, which is common for fluids with larger Prandtl numbers [13].

4.3. **Heat transfer.** The heat transfer across the inner and outer spherical shell provides an overall quantitative result to compare the different methods of solution. It is evaluated according to eq.(25) for all regimes and given in Table 3.

Notable is a Nu value smaller than unity for the regime (I) evaluated by the PSM and FEM techniques. Indeed, this result is, from a first point of view, surprising, as this indicates a suppressed conductive heat transport. However, there is a physical explanation, that relates to the forcing parameters. In regime (I) $Ra_E = 0$ neither electric force nor dielectric heating is present. The reason for $Nu < 1$ relates to the rotational forcing and is explained by the centrifugal buoyancy force, see eq.(15) and the applied non-uniformly heated boundary condition, see Figure 2. Colder, more dense fluid may then be displayed outward away from the rotational axis, and convection can occur by the centrifugal buoyancy force explaining the inward bending and outward bending of the temperature isotherms mentioned in Section 4.1.

The FVM technique was not able to recover a Nusselt number below unity for this particular case of regime (I) and has overestimated the Nusselt number compared to the FEM and PSM techniques. However, we have tested larger values of rotational forcing and different aspect ratios where the FVM technique showed values smaller than unity, recovering the FEM and PSM technique for Nu values smaller than unity. However, the Nusselt number increases with the Rayleigh number and is consistent throughout all methods. Another noticeable fact is a difference in the Nusselt number at the inner and outer shell caused by the dielectric loss of the alternating electric field heating the fluid inside the gap. Hence, the combination of the applied constant boundary temperature results in an increased heat flux through the domain caused by dielectric heating. The regimes (II) and (III) have a slight difference between the FVM and the other methods when the Rayleigh number and Taylor number increase. Both methods, the PSM and FEM, provide a small error to one another, where the FEM uses shape functions to describe the solution and treats the gradient on the curved hexahedron mesh structure better than a central differencing scheme. This may explain the difference in the inner and outer Nusselt numbers with the inner having a smaller error compared to the PSM and FEM methods than the outer Nusselt number. In addition, one has to note that the inner and outer cell sizes differ from one another as the mesh is uniformly produced having the same cell numbers at the inner and outer shell boundaries reducing the accuracy of the gradient calculation. A cell distribution with uniform element size would may provide an improved solution. However, the overall error remains at about 1% which is acceptable and proves the validity of the FVM solver.

5. **Concluding remarks**

An FVM solver using the OpenFOAM® ecosystem was prepared to solve the influence of an electric field on a rotating dielectric working fluid confined in a spherical shell. The arising convective flow was benchmarked using the basic flow states of three regimes given by Travnikov et al. [13]. These regimes occur as a result of the competition between the DEP force, Coriolis, and centrifugal forces and are steady, axisymmetric, and equatorially symmetric. This avoids spatial and temporal averaging, as the uncertainty can be directly evaluated and compared with one another, which makes the numerical solutions well suited for a benchmark exercise of different computational methods.

The OpenFOAM® solver was compared with a commercially available FEM [45] solver and a custom-coded PSM [22] solver. The results show well-matched qualitative and quantitative results when compared to the FEM and PSM techniques, with errors in the order of 1% or less. However, the OpenFOAM®

solver requires significantly more computational resources when compared to the commercial FEM. Despite the higher computational costs, the validation of the solver enables the investigation of more complex geometries without significant code development where the PSM method reaches its limitation. In addition, the solver is also able to compute multiregion and multiphysics to model complex flow from an engineering perspective.

The OpenFOAM® solver is made available via GitHub; see the repository link at the top of the document. This provides further development of the solver in improving the computational efforts and the addition of multiphysics to the solver for further fluid flow phenomena in electrohydrodynamics.

Acknowledgements

We would like to express our gratitude to the Resource Allocation Board that provided the computational time on the supercomputer Lise and Emmy at NHR@ZIB and NHR@Göttingen as part of the NHR infrastructure.

Funding This work is supported by the Bundesministerium für Wirtschaft und Klimaschutz (BMWK) via the German Space Administration (DLR) with grant no. 50WM1841, 50WM2141 and 50WM2441 and by the Deutsche Forschungsgemeinschaft (DFG) with grant no. TR 986/6-3. The numerical calculations were conducted with computing resources of the National High Performance (NHR) Computing infrastructure that received the funding to the project number bbi00021.

Author Contributions: Conceptualisation, Y.G.; methodology, Y.G., P.S. and V.T.; software, Y.G., P.S. and V.T.; validation, P.S. and V.T.; formal analysis, Y.G. and P.S.; investigation, Y.G. and P.S.; resources, P.S.; data curation, Y.G.; writing—original draft preparation, Y.G.; writing—review and editing, P.S.; visualisation, Y.G.; supervision, P.S. and C.E.; project administration, P.S. and C.E.; funding acquisition, P.S. and C.E.; All authors have read and agreed to the published version of the manuscript.

References

[1] I. Mutabazi, H. N. Yoshikawa, M. T. Fogaing, V. Travnikov, O. Crumeyrolle, B. Futterer, and C. Egbers, "Thermo-electro-hydrodynamic convection under microgravity: A review," *Fluid Dynamics Research*, vol. 48, no. 6, p. 061413, Nov. 2016.

[2] H. Senftleben and W. Braun, "Der Einfluß elektrischer Felder auf den Wärmestrom in Gasen," *Zeitschrift für Physik*, vol. 102, no. 7, pp. 480–506, Jul. 1936.

[3] H. Senftleben and J. Pietzner, "Die Einwirkung magnetischer Felder auf das Wärmeleitvermögen von Gasen. I," *Annalen der Physik*, vol. 408, pp. 907–929, Jan. 1933.

[4] H. Senftleben, "Über den Einfluß von magnetischen und elektrischen Feldern auf den Wärmestrom in Gasen," *Zeitschrift für Physik*, vol. 74, no. 11, pp. 757–769, Nov. 1932.

[5] H. N. Yoshikawa, C. Kang, I. Mutabazi, F. Zaussinger, P. Haun, and C. Egbers, "Thermoelectrohydrodynamic convection in parallel plate capacitors under dielectric heating conditions," *Physical Review Fluids*, vol. 5, no. 11, p. 113503, Nov. 2020.

[6] H. N. Yoshikawa, O. Crumeyrolle, and I. Mutabazi, "Dielectrophoretic force-driven thermal convection in annular geometry," *Physics of Fluids*, vol. 25, no. 2, p. 024106, Feb. 2013.

[7] H. N. Yoshikawa, M. Tadie Fogaing, O. Crumeyrolle, and I. Mutabazi, "Dielectrophoretic Rayleigh-Bénard convection under microgravity conditions," *Physical Review E*, vol. 87, no. 4, p. 043003, Apr. 2013.

[8] V. Travnikov, C. Egbers, and R. Hollerbach, "The geoflow-experiment on ISS (Part II): Numerical simulation," *Advances in Space Research*, vol. 32, no. 2, pp. 181–189, Jul. 2003.

[9] V. Travnikov, F. Zaussinger, P. Beltrame, and C. Egbers, "Influence of the temperature-dependent viscosity on convective flow in the radial force field," *Physical Review E*, vol. 96, no. 2, p. 023108, 2017.

[10] B. Futterer, M. Gellert, Th. von Larcher, and C. Egbers, "Thermal convection in rotating spherical shells: An experimental and numerical approach within GeoFlow," *Acta Astronautica*, vol. 62, no. 4, pp. 300–307, Feb. 2008.

[11] B. Futterer, C. Egbers, N. Dahley, S. Koch, and L. Jehring, "First identification of sub- and supercritical convection patterns from 'GeoFlow', the geophysical flow simulation experiment integrated in Fluid Science Laboratory," *Acta Astronautica*, vol. 66, no. 1, pp. 193–200, Jan. 2010.

[12] V. Travnikov, F. Zaussinger, P. Haun, and C. Egbers, "Influence of dielectrical heating on convective flow in a radial force field," *Physical Review E*, vol. 101, no. 5, p. 053106, May 2020.

[13] V. Travnikov and C. Egbers, "Numerical investigation of atmospherelike flows in a spherical geometry," *Physical Review E*, vol. 104, no. 6, p. 065110, Dec. 2021.

[14] C. Kang, A. Meyer, H. N. Yoshikawa, and I. Mutabazi, "Numerical simulation of circular Couette flow under a radial thermo-electric body force," *Physics of Fluids*, vol. 29, no. 11, p. 114105, Nov. 2017.

[15] ——, "Thermoelectric convection in a dielectric liquid inside a cylindrical annulus with a solid-body rotation," *Physical Review Fluids*, vol. 4, no. 9, p. 093502, Sep. 2019.

[16] C. Kang, A. Meyer, H. Yoshikawa, and I. Mutabazi, "Numerical study of thermal convection induced by centrifugal buoyancy in a rotating cylindrical annulus," *Physical Review Fluids*, vol. 4, Apr. 2019.

[17] F. Zaussinger, P. Haun, P. S. B. Szabo, V. Travnikov, M. Al Kawwas, and C. Egbers, "Rotating spherical gap convection in the GeoFlow International Space Station (ISS) experiment," *Physical Review Fluids*, vol. 5, no. 6, p. 063502, Jun. 2020.

[18] P. S. Szabo, Y. Gaillard, F. Zaussinger, and C. Egbers, "Thermo-electrohydrodynamic convection in a differentially heated shell with electric central force field," *PAMM*, vol. 23, no. 1, p. e202200121, 2023.
[19] Y. Gaillard, P. Szabo, V. Travnikov, and C. Egbers, "Thermo-Electrohydrodynamic Convection in a Rotating Shell with Central Force Field," Rochester, NY, Jun. 2023.
[20] P. Gerstner and V. Heuveline, "Finite element approximation of dielectrophoretic force driven flow problems," *ESAIM: Mathematical Modelling and Numerical Analysis*, vol. 57, no. 3, pp. 1691–1729, 2023.
[21] Y. Gaillard, P. S. Szabo, V. Travnikov, and C. Egbers, "Thermo-electrohydrodynamic convection in a rotating shell with central force field," *International Journal of Heat and Mass Transfer*, vol. 218, p. 124760, 2024.
[22] R. Hollerbach, "A spectral solution of the magneto-convection equations in spherical geometry," *International Journal for Numerical Methods in Fluids*, vol. 32, no. 7, pp. 773–797, 2000.
[23] ——, "Instabilities of the stewartson layer part 1. the dependence on the sign of," *Journal of Fluid Mechanics*, vol. 492, pp. 289–302, Oct 2003.
[24] T. Gastine, J. Wicht, and J. Aubert, "Scaling regimes in spherical shell rotating convection," *Journal of Fluid Mechanics*, vol. 808, pp. 690–732, Dec. 2016.
[25] J. Aubert, T. Gastine, and A. Fournier, "Spherical convective dynamos in the rapidly rotating asymptotic regime," *Journal of Fluid Mechanics*, vol. 813, pp. 558–593, Feb. 2017.
[26] B. Futterer, R. Hollerbach, and C. Egbers, "GeoFlow: 3D numerical simulation of supercritical thermal convective states," *Journal of Physics: Conference Series*, vol. 137, no. 1, p. 012026, Nov. 2008.
[27] B. Futterer, A. Krebs, A.-C. Plesa, F. Zaussinger, R. Hollerbach, D. Breuer, and C. Egbers, "Sheet-like and plume-like thermal flow in a spherical convection experiment performed under microgravity," *Journal of fluid mechanics*, vol. 735, pp. 647–683, 2013.
[28] B. Futterer, S. Koch, and C. Egbers, "Traveling waves in low and intermediate rotating spherical shell convection," *Journal of Physics: Conference Series*, vol. 318, no. 3, p. 032006, Dec. 2011.
[29] B. Futterer, N. Dahley, S. Koch, N. Scurtu, and C. Egbers, "From isoviscous convective experiment 'geoflow i'to temperature-dependent viscosity in 'geoflow ii'—fluid physics experiments on-board iss for the capture of convection phenomena in earth's outer core and mantle," *Acta Astronautica*, vol. 71, pp. 11–19, 2012.
[30] "OpenFOAM: User Guide," https://www.openfoam.com/documentation/guides/latest/doc.
[31] F. Zaussinger, P. Canfield, A. Froitzheim, V. Travnikov, P. Haun, M. Meier, A. Meyer, P. Heintzmann, T. Driebe, and C. Egbers, "Atmoflow-investigation of atmospheric-like fluid flows under microgravity conditions," *Microgravity Science and Technology*, vol. 31, no. 5, pp. 569–587, 2019.
[32] R. Chand, "Electro-thermal convection in a Brinkman porous medium saturated by nanofluid," *Ain Shams Engineering Journal*, vol. 8, no. 4, pp. 633–641, Dec. 2017.
[33] L. D Landau, E. M Lifshits, and L. P. Pitaevskiĭ, *Electrodynamics of Continuous Media*. Oxford: Pergamon Press Ltd, 1984.
[34] R. J. Turnbull, "Electroconvective instability with a stabilizing temperature gradient. ii. experimental results," *The Physics of Fluids*, vol. 11, no. 12, pp. 2597–2603, 1968.
[35] A. Meyer, H. Yoshikawa, P. S. Szabo, M. Meier, C. Egbers, and I. Mutabazi, "Thermoelectric instabilities in a circular couette flow," *Philosophical Transactions of the Royal Society A*, vol. 381, no. 2243, p. 20220139, 2023.
[36] P. H. Roberts, "Electrohydrodynamic convection," *The Quarterly Journal of Mechanics and Applied Mathematics*, vol. 22, no. 2, pp. 211–220, 1969.
[37] P. J. Stiles, "Electro-thermal convection in dielectric liquids," *Chemical Physics Letters*, vol. 179, no. 3, pp. 311–315, Apr. 1991.
[38] F. Zaussinger, P. Haun, M. Neben, T. Seelig, V. Travnikov, C. Egbers, H. Yoshikawa, and I. Mutabazi, "Dielectrically driven convection in spherical gap geometry," *Physical Review Fluids*, vol. 3, no. 9, p. 093501, Sep. 2018.
[39] R. J. Turnbull, "Effect of Dielectrophoretic Forces on the Bénard Instability," *The Physics of Fluids*, vol. 12, no. 9, pp. 1809–1815, Sep. 1969.
[40] C. Kang and I. Mutabazi, "Dielectrophoretic buoyancy and heat transfer in a dielectric liquid contained in a cylindrical annular cavity," *Journal of Applied physics*, vol. 125, no. 18, 2019.
[41] F. H. Busse, "Thermal instabilities in rapidly rotating systems," *Journal of Fluid Mechanics*, vol. 44, no. 3, pp. 441–460, 1970.
[42] J. Zhong, D. Wang, and C. Sun, "From sheared annular centrifugal rayleigh–bénard convection to radially heated taylor–couette flow: exploring the impact of buoyancy and shear on heat transfer and flow structure," *Journal of Fluid Mechanics*, vol. 972, p. A29, 2023.
[43] D. J. Tritton, *Physical fluid dynamics*. Springer Science & Business Media, 2012.
[44] Joel H. Ferziger, Milovan Perić, and Robert L. Street, *Numerische Strömungsmechanik*. Springer, 2020.
[45] COMSOL Multiphysics ®, "User's Guide, Version 4.4," November 2013. [Online]. Available: http://www.comsol.com
[46] G. De Vahl Davis, "Natural convection of air in a square cavity: A bench mark numerical solution," *International Journal for Numerical Methods in Fluids*, vol. 3, no. 3, pp. 249–264, May 1983.
[47] P. Szabo, M. Beković, and W.-G. Früh, "Infrared thermography of wall temperature distribution caused by convection of magnetic fluid," *International Journal of Thermal Sciences*, vol. 134, pp. 129–139, Dec. 2018.